AGU PUBLICATIONS

JGR

Journal of Geophysical Research: Earth Surface

RESEARCH ARTICLE
10.1002/2014JF003423

Key Points:
- Large eddy simulation of flow and solute transport in a forested stream
- Simulation results for time series of solute transport are validated using field data
- Simulations revealed details of mechanisms by which tracer are trapped in local areas

Supporting Information:
- Movies S1–S4 captions
- Movie S1
- Movie S2
- Movie S3
- Movie S4

Correspondence to:
F. Sotiropoulos,
fotis.sotiropoulos@stonybrook.edu

Citation:
Khosronejad, A., A. T. Hansen, J. L. Kozarek, K. Guentzel, M. Hondzo, M. Guala, P. Wilcock, J. C. Finlay, and F. Sotiropoulos (2016), Large eddy simulation of turbulence and solute transport in a forested headwater stream, *J. Geophys. Res. Earth Surf.*, *121*, 146–167, doi:10.1002/2014JF003423.

Received 31 DEC 2014
Accepted 28 DEC 2015
Accepted article online 5 JAN 2016
Published online 25 JAN 2016

Large eddy simulation of turbulence and solute transport in a forested headwater stream

A. Khosronejad[1], A. T. Hansen[1], J. L. Kozarek[1], K. Guentzel[2], M. Hondzo[1], M. Guala[1], P. Wilcock[3], J. C. Finlay[4], and F. Sotiropoulos[5,6]

[1]Saint Anthony Falls Laboratory and Department of Civil Engineering, University of Minnesota, Twin Cities, Minneapolis, Minnesota, USA, [2]Anoka Conservation District, Minneapolis, Minnesota, USA, [3]Department of Civil and Environmental Engineering, Utah State University, Logan, Utah, USA, [4]Saint Anthony Falls Laboratory and Department of Ecology, Evolution, and Behavior, University of Minnesota, Twin Cities, St. Paul, Minnesota, USA, [5]Saint Anthony Falls Laboratory and Department of Civil Engineering, University of Minnesota, Twin Cities, Minneapolis, Minnesota, USA, [6]Dean, College of Engineering and Applied Sciences and Professor of Civil Engineering, State University of New York at Stony Brook, Stony Brook, New York, USA

Abstract The large eddy simulation (LES) module of the Virtual StreamLab (VSL3D) model is applied to simulate the flow and transport of a conservative tracer in a headwater stream in Minnesota, located in the south Twin Cities metropolitan area. The detailed geometry of the stream reach, which is ~135 m long, ~2.5 m wide, and ~0.15 m deep, was surveyed and used as input to the computational model. The detailed geometry and location of large woody debris and bed roughness elements up to ~0.1 m in size were also surveyed and incorporated in the numerical simulation using the Curvilinear Immersed Boundary approach employed in VSL3D. The resolution of the simulation, which employs up to a total of 25 million grid nodes to discretize the flow domain, is sufficiently fine to directly account for the effect of large woody debris and small cobbles (on the streambed) on the flow patterns and transport processes of conservative solutes. Two tracer injection conditions, a pulse and a plateau release, and two cross sections of measured velocity were used to validate the LES results. The computed results are shown to be in good agreement with the field measurements and tracer concentration time series. To our knowledge, the present study is the first attempt to simulate via high-resolution LES solute transport in a natural stream environment taking into account a range of roughness length scales spanning an order of magnitude: from small cobbles on the streambed (~0.1 m in diameter) to large woody debris up to ~3 m long.

1. Introduction

Stream channel geomorphic features such as side pools, meander bends, flow obstructions (e.g., boulders and large woody debris), and recirculation zones generate heterogeneity in streamflow conditions that, in turn, drive spatial variability in biological community distribution and ecosystem processes. The complex flow conditions created by geomorphic features within a stream reach pose a significant challenge to numerical methods for three major reasons: (i) the geometry of streams, which typically include large woody debris and other streambed roughness elements (e.g., cobbles and boulders), is highly complex; (ii) the structure of turbulence, which is dominated by geometry-induced, dynamically rich, highly three-dimensional (3-D), and energetic coherent structures that produce turbulence and govern the transport of momentum, scalars, and sediment; and (iii) the need for high-fidelity and, thus, computationally intensive, coherent structure-resolving simulations to accurately resolve the ensuing turbulent flows. Because of these challenges, most studies relating to ecosystem function and processes with stream channel hydraulics have employed analytical, one-dimensional, or two-dimensional models despite evidence that the underlying biogeochemical processes exhibit heterogeneities to submeter scales [*Tank et al.*, 2000; *De Smedt et al.*, 2005; *Khosronejad*, 2009; *Schmalle and Rehmann*, 2014].

Streamflow heterogeneity has been shown to be a significant driver of many ecosystem processes such as community patch distribution, carbon deposition, and bacterially mediated nutrient cycling processes such as denitrification and methylmercury production [*Hart and Finelli*, 1999; *Branfireun and Roulet*, 2002; *Bernhardt et al.*, 2003]. For example, localized flow conditions may control macroinvertebrate distribution patchiness through both dispersal and habitat suitability [*Lancaster and Hildrew*, 1993; *Hart and Finelli*, 1999; *Ceola et al.*,

2014; *Morales et al.*, 2006]. Similarly, denitrification, a bacterial process through which nitrate and nitrite are reduced to various forms of nitrogen gas, has been shown to occur in concentrated, subreach "hot spots" of activity [*Tiedje et al.*, 1982; *McClain et al.*, 2003; *Groffman et al.*, 2009]. Areas of the stream channel with relatively lower velocities (or longer residence times) allow for enhanced contact with bed sediments for biogeochemical processing of dissolved solutes [e.g., nutrients or contaminants; *Ensign and Doyle*, 2005; *Opdyke et al.*, 2006] or particulates [e.g., organic material; *Bernhardt et al.*, 2003] and provide diversity in habitat conditions [*Fausch and White*, 1981].

The effects of geomorphically induced streamflow complexity on biogeochemical processes has primarily been evaluated using a combination of surface tracers and simplified storage zone models [*Baker et al.*, 2011; *Kaufmann and Faustini*, 2012]. Limitations of these methods include the following: (i) differences in interpretation between tracer methods for instantaneous and constant rate tracer for subreach residence time distributions [*Gooseff et al.*, 2007], (ii) difficulty separating the effect of storage zone type between surface storage and hyporheic storage [*Runkel et al.*, 2003], (iii) difficulty in identifying the influence of individual surface storage zones [*Gooseff et al.*, 2011], and (iv) reach length dependence on simulated exchange [*Gooseff et al.*, 2013]. Such simplified methods can capture reach-averaged process rates through parameterization but cannot elucidate whether the processes are constant across the reach or primarily occurring at discrete locations with higher activity rates. Thus, predicting how channel geomorphology drives stream ecosystem processes requires characterizing the complex 3-D hydraulic conditions present in natural streams.

There are several computational studies of turbulent flow and transport processes in waterways and reservoir environments using 3-D Reynolds-averaged Navier-Stokes (RANS) models [*Brian*, 1961; *Burnett and Frind*, 1987; *Demuren and Rodi*, 1986; *Cerco and Cole*, 1993; *Hoch and Garreau*, 1998; *Reckhow and Chapra*, 1999; *Park et al.*, 2005; *Cerco et al.*, 2006; *Ambrose et al.*, 2009; *McDonald et al.*, 2012; *Cerco et al.*, 2013]. Such models, however, due to their inherent diffusive effects, cannot resolve the energetic coherent structures that dominate flows in streams and only account for the effects of geometrical heterogeneities in a statistical sense. Thus, we argue that high-fidelity computational models that can resolve the 3-D details of the turbulent flow and directly account for the effects of spatial heterogeneities and geometric complexity of streambeds are critical for identifying channel features that promote desirable ecosystem services and quantify the subreach contribution of biogeochemical hot spots.

With increasing computing power and advances in computational fluid dynamics algorithms, it is now possible to computationally investigate turbulent mixing and convection of solutes in more complex channels and with turbulence-resolving models. *Kirkpatrick and Armfield* [2005] employed experimental observations and carried out large eddy simulation (LES) to investigate salt transport near a cavity in a prismatic experimental flume. *Chang et al.* [2007] and *McCoy et al.* [2007] also employed LES to simulate the mass transport momentum transport in a straight flume with installed groins. A more detailed overview of recent LES applications to simulate turbulent flows in open channels can be found in *Stoesser* [2014].

Applications of LES to study turbulent flow processes in natural stream environments with complex bathymetry and embedded structures have also been reported in the literature. *Kang et al.* [2011] developed a powerful computational framework, the Virtual StreamLab (VSL3D), capable of simulating turbulent flows in meandering streams and rivers using the Curvilinear Immersed Boundary (CURVIB) method of *Ge and Sotiropoulos* [2007] coupled with wall models for reconstructing velocity boundary conditions near the streambed. *Kang and Sotiropoulos* [2011] employed the same model to study the mechanisms that lead to multicellular secondary flow patterns in natural meander bends. In another study VSL3D was employed to underscore the limitations of isotropic RANS models for resolving the structure of secondary flows in natural bends and demonstrate the need for LES. More recently, the VSL3D has been further extended to incorporate free surface effects [*Kang and Sotiropoulos*, 2012a] and also develop a coupled hydrodynamic formulation for simulating sand wave dynamics across a range of scales [*Khosronejad et al.*, 2014, 2015; *Khosronejad and Sotiropoulos*, 2014].

In this paper we adapt and employ the VSL3D code to simulate turbulent flow and solute transport processes in a natural stream with no need of the following: (i) calibrating or tuning the model, (ii) simplifying the natural geometry of the stream, or (iii) ignoring the presence of immersed objects (e.g., large woody debris) in the stream. To do so, we take into account natural large-scale roughness elements such as boulders, rocks, and large woody debris. By analyzing the simulation results for the flow and solute concentration field, we attempt to better understand the important mechanisms in solute transport in natural streams.

The streambed bathymetry and all morphological bathymetric features of the site were obtained from a field campaign and used to create a digital elevation model of the site, which is used as input into the VSL3D code. The computed results are compared with field measurements taken during two consecutive injections of a conservative tracer (pulse and plateau releases of NaCl). The simulated flow fields are subsequently employed to systematically evaluate the effect of stream bank geometry, stream bifurcation, and large flow obstructions (emergent rocks and logs) on local- and reach-scale residence times of the conservative solute. The results of this study demonstrate for the first time the enormous potential of high-fidelity LES of natural streamflows as a powerful tool for exploring the effects of spatial heterogeneities on solute residence times, the downstream persistence of topographically induced flow structures, and testing predictions or hypotheses for hot spots of ecological processes.

The paper is organized as follows. First, we introduce briefly the VSL3D hydrodynamic model followed by the description of the experimental procedures we used to measure the streambed geometry, flow velocity, and tracer concentration in the stream. Subsequently, we present the simulation and field measurement results of the flow and concentration field. This is followed by discussing the effects of specific heterogeneities (e.g., bifurcations, large woody debris, and large-scale roughness elements) on the residence time of the conservative tracer. Finally, in the last section, we discuss future extension of the research findings to simulate nonconservative tracer transport.

2. The VSL3D Model

We consider incompressible and turbulent flow of water which is governed by the spatially filtered continuity and Navier-Stokes equations. The transformed governing equations for the resolved flow field in nonorthogonal, generalized, curvilinear coordinates read in compact tensor notation as follows ($i = 1, 2,$ or 3 and repeated indices, i.e., j, k, l, imply summation over 1 to 3):

$$J\frac{\partial U^j}{\partial \xi^j} = 0 \tag{1}$$

$$\frac{1}{J}\frac{\partial U^i}{\partial t} = \frac{\xi_l^i}{J}\left(-\frac{\partial}{\partial \xi^j}\left(U^j u_l\right) + \frac{1}{Re}\frac{\partial}{\partial \xi^j}\left(\frac{G^{jk}}{J}\frac{\partial u_l}{\partial \xi^k}\right) - \frac{\partial}{\partial \xi^j}\left(\frac{\xi_l^j p}{J}\right) - \frac{\partial \tau_{lj}}{\partial \xi^j}\right) \tag{2}$$

where J is the Jacobian of the geometric transformation given by $J = \left|\partial(\xi^1, \xi^2, \xi^3)/\partial(x_1, x_2, x_3)\right|$; x_1, x_2, and x_3 are the streamwise, spanwise, and vertical coordinates, respectively; $\xi_l^i = \partial \xi^i / \partial x_l$ are the transformation metrics; u_l is the lth Cartesian velocity component; $U^j = (\xi_m^j/J)u_m$ is the contravariant volume flux; $G^{jk} = \xi_l^j \xi_l^k$ are the components of the contravariant metric tensor; p is the pressure; $Re = \rho U_m H_m/\mu$ is the Reynolds number; U_m is the mean flow velocity; H_m is the mean flow depth; μ is the dynamic viscosity; ρ is the density of water-solute mixture, which is assumed to be constant and equal to the density of water; and τ_{lj} is the subgrid stress tensor for LES model. The subgrid-scale stresses are modeled using the dynamic Smagorinsky model implemented as described in detail in *Kang and Sotiropoulos* [2011].

The volume fraction of conservative tracer (ψ) is modeled as a passive scalar whose transport is governed by the following convection-diffusion equation [*Chou and Fringer*, 2008, 2010; *Kraft et al.*, 2011; *Khosronejad and Sotiropoulos*, 2014]:

$$\frac{1}{J}\frac{\partial(\rho\psi)}{\partial t} + \frac{\partial(\rho U^j \psi)}{\partial \xi^j} = \frac{\partial}{\partial \xi^j}\left((\mu + \sigma^* \mu_t)\frac{G^{jk}}{J}\frac{\partial \psi}{\partial \xi^k}\right) \tag{3}$$

where σ^* is the Schmidt number (= 0.75) [*Khosronejad et al.*, 2008] and μ_t is the eddy viscosity obtained from LES model [*Kang and Sotiropoulos*, 2011].

Third-order accurate weighted essentially nonoscillatory (WENO) scheme [*Jiang and Shu*, 1996] and second-order central differencing schemes are employed for the spatial discretization of advection and diffusion terms in the solute concentration transport equation (equation (3)), respectively. Additionally, the second-order backward differencing scheme is used for the time integration. The convection-diffusion equation is solved using the fully implicit Jacobian-free Newton method at every time step after the velocity fields are obtained by the fractional step method [*Kang et al.*, 2011].

The details of the numerical method for solving the flow, solute transport, and turbulence closure governing equations in complex domains have already been documented extensively elsewhere [*Ge and Sotiropoulos*,

2007; *Borazjani et al.*, 2008; *Kang et al.*, 2011; *Khosronejad and Sotiropoulos*, 2014], and only a brief summary of key elements of the method will be given here. The governing equations for resolved flow field are discretized in space on a hybrid staggered/nonstaggered grid arrangement [*Gilmanov and Sotiropoulos*, 2005; *Ge and Sotiropoulos*, 2007] using second-order accurate central differencing for the convective terms along with second-order accurate, three-point central differencing for the divergence, pressure gradient, and viscous-like terms. Additionally, the WENO scheme [*Jiang and Shu*, 1996] and second-order central differencing schemes are employed for the spatial discretization of advection and diffusion terms of the solute transport equation, respectively. The time derivatives are discretized using second-order backward differencing [*Kang et al.*, 2011]. The discrete flow equations are integrated in time using an efficient, second-order accurate fractional step methodology coupled with a Jacobian-free, Newton-Krylov solver for the momentum equations and a Generalized Minimal Residual (GMRES) solver enhanced with the multigrid method as a preconditioner for the Poisson equation. For additional details, the reader is referred to *Ge and Sotiropoulos* [2007], *Borazjani et al.* [2008], and *Kang et al.* [2011].

The geometrically complex computational domain of Eagle Creek is handled using the sharp interface CURVIB method of *Ge and Sotiropoulos* [2007] as extended to turbulent flows by *Kang et al.* [2011]. In the CURVIB method, instead of using a boundary-conforming mesh to describe the shape and geometry of the streambed and immersed rigid objects, we treat nonmonotonic streambed bathymetry and large woody debris as sharp interfaces, and boundary conditions are reconstructed at curvilinear grid nodes in the immediate vicinity of the boundary using the wall model approach described in detail in *Kang et al.* [2011]. In the present work, the computational domain consists of a meandering-like channel that outlines the stream under consideration and is sufficiently deep to contain the entire interface of water and rigid walls throughout the stream. The computational domain is discretized with a boundary-fitted curvilinear mesh, while the interface of water and rigid bed, banks, and large woody debris is discretized with an unstructured grid and immersed in the background domain as a sharp interface in accordance with the CURVIB formulation. According to the CURVIB formulation, the governing equations are solved at the background grid nodes in the fluid phase (fluid nodes) with boundary conditions specified at fluid nodes in the immediate vicinity of the rigid objects and water interfaces (i.e., immersed boundary (IB) nodes). Flow and tracer transport are resolved in the fluid phase (i.e., flow over and under immersed large woody debris is resolved), while all nodes inside the stream banks, streambed, cobbles, and large woody debris domains (denoted as external nodes) are blanked out from the computations. The computed flow field at each time step will be used to solve for the concentration field of conservative tracer using the convection-diffusion equation (equation (3)).

3. Study Area: Eagle Creek

Eagle Creek is a first-order tributary of the Minnesota River, located in Savage, MN. Our study site is an approximately 135 m long reach of the East Branch of Eagle Creek with an average width of approximately $B \sim 2.5$ m. The riparian area is forested with vegetated banks, and the streambed substrate is primarily sand with a limited section of bedrock. The study area contains geometrically complex features such as a small island, large woody debris, boulders, and several mild and sharp meander bends. The stream is primarily groundwater fed, with a relatively constant base flow discharge throughout the summer. The discharge at the time of this study (July 2012) was 36 L s^{-1}.

Although Eagle Creek is groundwater fed, the stream reach in this study was chosen to have minimal groundwater inputs. This was confirmed via longitudinal temperature profiles, multiple discharge measurements, and tracer mass balance analysis. Given the small size of the stream, hyporheic storage within the study reach was also negligible [less than 0.5% of total hydraulic retention as reported by *Stofleth et al.* 2008] and therefore was not accounted for in the simulations.

4. Description of Field Surveying Procedure

To carry out site-specific high-resolution LES for the flow and conservative tracer transport in Eagle Creek high-resolution geometry, data are required to adequately represent complex features such as large woody debris and boulders (see Figure 1). Streambed, bank, and water surface geometry were surveyed using a total station (Sokkia SET 330R) to create a detailed stream bathymetry map. Individual pieces of large wood debris were measured and surveyed separately. Roughness and streambed properties (e.g., bedrock, gravel,

Figure 1. Representative photographs of Eagle Creek with (top) a large wood piece and (bottom) highly complex bed roughness elements near the outlet section of the reach. Flow in both photographs is from bottom to top.

sand bedforms, vegetation, and organic deposition areas) were also surveyed and classified by visually similar streambed roughness. The water surface elevation was also surveyed at the time of the field data collection.

4.1. Stream Topography and Water Surface

Survey data (over 2800 points) collected from seven total station locations were tied together using 15 benchmarks along the stream (Figure 2). The standard deviation of repeat survey measurements of all 15 benchmarks was less than 1 cm. To represent the complex topography of Eagle Creek, survey points were topographically stratified [*Bangen et al.*, 2014] with higher point densities at breaks in slope (along banks) and in areas of complex topography. Complex topography in this stream consisted of two sections of rocks and boulders (>~0.2 m in diameter) that were represented in the survey by collecting a point at the apex(es) of each boulder and a minimum of three points around the base [*Kozarek et al.*, 2010; *Resop et al.*, 2012]. Within the streambed, maximum point spacing was approximately 0.5 m in topographically flat areas. Points were collected in the floodplain (at least 1 m to 2 m away from the top of bank) to ensure appropriate interpolation along the stream banks. Large woody debris were surveyed separately (see Figure 3). To recreate the geometry of large woody debris, the diameter was recorded along with survey points (location and elevation) along the midline of the top of each piece. Small wood pieces (i.e., branches and sticks with a diameter smaller than approximately 10 cm) and the minimal aquatic vegetation were removed prior to topographical characterization of the site.

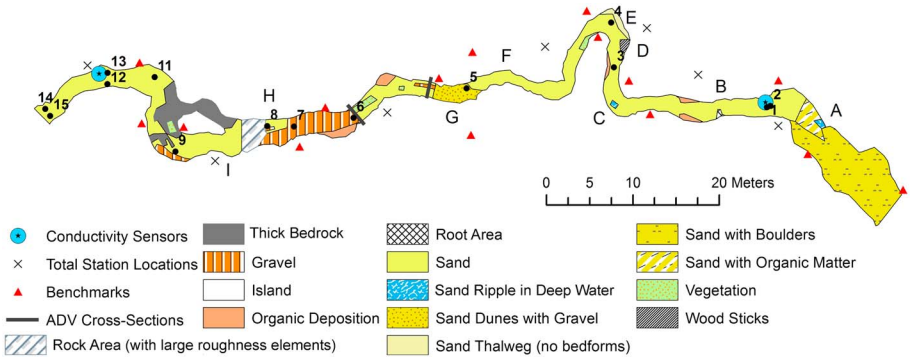

Figure 2. Surveyed bed roughness map and locations of different measuring apparatuses. Shading represents regions of visually similar bed roughness. Numbers and letters indicate locations of grain size samples (Table 2) and bedform field notes (Table 1), respectively. This map is used to extract the local effective roughness height for the flow field simulations. Flow is from left to right.

The surveyed bathymetry of Eagle Creek bed and large woody debris are shown in Figure 3. The measured bathymetry in Figure 3 illustrates the level of resolution of the different streambed and large wood features. The water surface elevation was also surveyed along the reach and is shown in Figure 3e.

4.2. Streambed Roughness

The boulders, cobbles, stream bank irregularities, large woody debris, and other streambed roughness elements larger than ~0.1 m were directly surveyed and resolved in the simulations (for details of computational grid size see section 6). The streambed roughness elements smaller than ~0.1 m, which are mainly associated with flat bed gravel roughnesses and migrating sand bedforms, were not surveyed. In order to account for such unresolved roughness elements in the simulations, we measured their characteristics and calculate their corresponding effective roughness height (k_s) to be taken into account in the simulations via the wall model

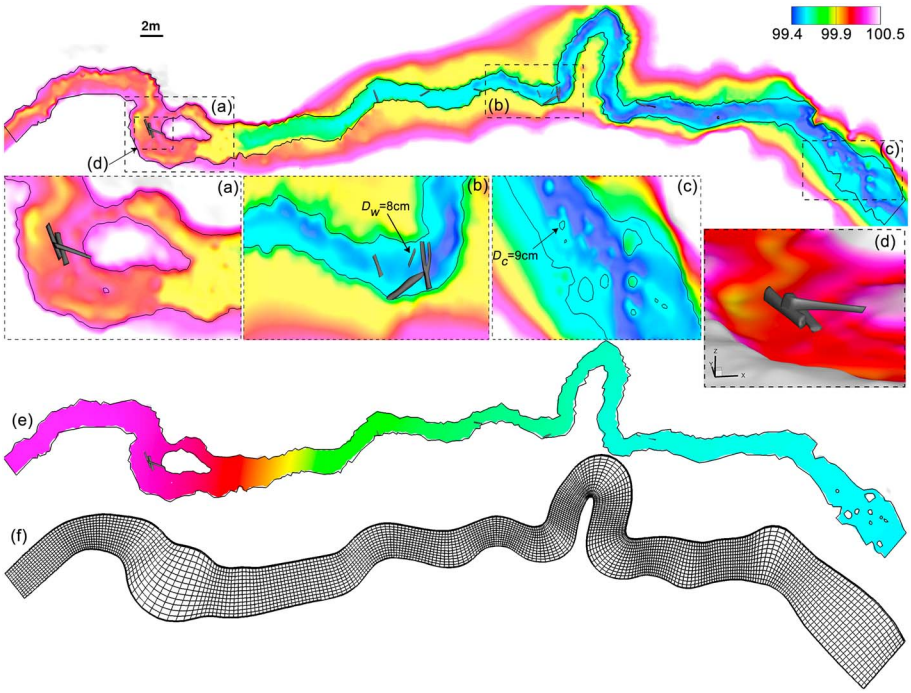

Figure 3. (a–d) Surveyed bathymetry of Eagle Creek, (e) measured water surface elevation, and (f) curvilinear grid system used for the simulations. Stream bathymetry includes the side walls, bed, cobbles, and 13 large woody debris pieces (in gray). D_w and D_c represent the diameter of the surveyed wood piece and cobble, respectively. For clarity only one out of the 10 computational grid cells is plotted in Figure 3f. Color scale shows contours of bed (Figures 3a–3d) and water surface elevation (Figure 3e) in meters (above an arbitrary datum), and flow is from left to right.

Table 1. Characteristics of the Bedforms Observed in Eagle Creek Based on the Regions Shown in Figure 2[a]

Region	Description	Bedform	Δ (cm)	λ (cm)
A	sand ripple	ripple	2	23
B	sand, center of stream	ripple	1.5	13
C	sand ripple	ripple	3	26
D	small sticks (diameter: 1–3 cm, length: ~40 cm)	flat bed	NA	NA
E	sand, flat bed (no bedforms)	flat bed	NA	NA
F	sand	ripple	2	7
G	sand with gravel	ripple	2	8
H	sand	ripple	1	5
I	sand	ripple	1	5

[a] Δ and λ represent the averaged amplitude and wavelength of the observed bedforms, respectively. NA: not available.

approach. To do so, an additional survey was conducted to map patches of different streambed roughness. Patches of visually similar bed material (e.g., sand, gravel, and organic matter) or bedforms (e.g., sand dunes) were surveyed along the entire study reach. Field notes documented bedform characteristics for different areas in Figure 2 that are represented in Table 1. Surface samples of bed material were collected by carefully retaining the top 0.01–0.02 m (equal to at least the size of the largest elements) of sediment in a 0.102 m diameter pipe. These samples were sieved in the laboratory for grain size distribution to obtain the local d_{50} of bed materials (Table 2). For the flat bed regions (Figure 2), the surface of the large woody debris, cobbles, and other resolved objects in the stream (Figure 3), k_s is set equal to $3d_{50}$ of the local bed material and for the regions of the stream in which bedforms are present, k_s is approximated locally using *Van Rijn* [1984] empirical equation and based on the measured bedforms characteristics as follows:

$$k_s = 3d_{90} + 1.1\Delta\left(1 - e^{\left(\frac{-25\Delta}{7.3h}\right)}\right) \tag{4}$$

where Δ is the amplitude of the measured bedforms and h is the local flow depth.

5. Field Measurements

We conducted two separate conservative tracer (NaCl) injection scenarios including a pulse release and a plateau release, which will be referred to as test cases A and B, respectively. The field measurements consisted of mean flow velocity components, turbulence statistics, and instantaneous solute concentration data.

Table 2. Characteristics of the Collected Samples of Bed Sediment Material From Eagle Creek Based on the Regions Shown in Figure 2

Sample	Sediment Type	d_{50} (mm)	d_{90} (mm)
1	sand (moderately sorted)	0.31	0.61
2	sand (moderately sorted)	0.31	0.73
3	sand (moderately sorted)	0.26	0.49
4	sand (moderately sorted)	0.29	0.61
5	sand/boulder (poorly sorted)	0.28	2.57
6	gravel (poorly sorted)	0.30	3.28
7	gravel (poorly sorted)	0.50	3.66
8	sand (moderately sorted)	0.26	0.48
9	sand/gravel (poorly sorted)	0.48	19.91
10	sand (moderately sorted)	0.36	0.98
11	sand (poorly sorted)	0.34	1.37
12	sand (moderately sorted)	0.31	0.71
13	sand (moderately sorted)	0.29	0.55
14	sand (moderately sorted)	0.26	0.61
15	sand (moderately sorted)	0.26	0.49

5.1. Conservative Tracer

Solute was injected approximately 20 m upstream from the inlet section of the simulation domain within a large zone of bedrock with shallow and well-mixed flow. Prior to the tracer experiments, rhodamine WT dye was injected into the stream at this location and measured at nine transects along the stream reach to determine an upstream measurement location that met the general assumption of well-mixed conditions; this ensures that a uniformly mixed tracer at the cross section of the domain inlet is, in fact, a reasonable assumption for the simulations [*Runkel*, 2015].

The plateau tracer experiment (test case B), consisting of an 8 h continuous constant rate injection of NaCl, was conducted in July 2012. A concentrated solution of NaCl tracer was continuously injected using a peristaltic pump at a rate of 9.2×10^{-3} L s^{-1} increasing the measured conductance from 650 μS/cm background to 745 μS/cm (i.e., 15% increase). Prior to experiments, the pump was calibrated in the St. Anthony Falls Laboratory (SAFL) using volume-duration measurements and was linear through a range of 0.4 to 1.1 L/min ($r^2 = 0.99, N = 6$). The injection rate was checked four times throughout the experiment and adjusted slightly once to ensure that pump rate was within 5% of the nominal value. Specific conductivity was measured at the upstream location at a 5 s sampling interval and at the downstream location at a 10 s interval. At both locations (shown in Figure 2), specific conductivity was measured using a Hydrolab Data Sonde 4A (Hach Company, Loveland, CO, USA) located in the stream thalweg, with the sensor oriented to face upstream, 0.03 m from the sediment-water interface.

The pulse tracer experiment (test case A) was also completed in July 2012 for which 13 L of NaCl solution, with a specific conductivity of 455 μS/cm, was released manually over 32 s with an injection rate of 4.06×10^{-1} L s^{-1} at the same injection location as was used for the plateau experiment. Similar to the plateau injection experiment, time series of specific conductivity were measured at the upstream and downstream locations (see Figure 2) using the same sensors in the same location and orientation.

All specific conductivity sensors were calibrated together at SAFL using a two-point calibration protocol prior to the experiments. The dependency of specific conductivity on the NaCl concentration (ψ) was linear throughout the range of 450 to 860 μS/cm ($r^2 = 0.99, N = 4$). The calibration relation was $\psi(\text{mg/L}) = 0.51\psi(\mu\text{S/cm}) - 31.608$.

5.2. Flow Field

Velocity measurements were collected at two cross sections using a 3-D Nortek Vectrino + acoustic Doppler velocimeter (ADV) at 200 Hz sampling frequency for 2 min. The ADV was attached to a leveled cross section adjustable in the vertical and cross-stream directions. Vertical ADV profiles were collected approximately every 0.25 m. Vertical ADV point spacing varied between 0.005 m and 0.05 m and was stratified to collect more measurements closer to the bed. Velocity data were postprocessed using the modified phase-space thresholding method [*Parsheh et al.*, 2010].

6. Computational Details

We simulated the two test cases A (pulse release) and B (plateau release) of the conservative tracer transport for which the flow condition was identical. The mean flow depth was $H_m = 0.15$ m, and the mean flow velocity was $U_m = 0.16$ m s^{-1} at the time of tracer experiments. The corresponding values of the Reynolds number and Froude number, based on the mean flow depth H_m and the bulk velocity U_m, are $Re = 25,000$ and $Fr = 0.13$, respectively. For both cases, we carried out LES of the turbulent flow and conservative tracer transport using the numerical method described in section 2.

At the inlet of the computational domain (i.e., the study reach within Eagle Creek) we prescribed fully turbulent flow, which is obtained by carrying out a separate LES for a virtual channel with (i) identical cross section of the inlet section (straightly extended 5 m upstream), (ii) flow conditions defined by the field measurements, and (iii) using periodic conditions in the streamwise direction. Once this LES reached the statistically stationary fully developed turbulent flow state, we stored a sufficiently long sample of the instantaneous velocity fields in order to use them as instantaneous inflow conditions for the LES of the full-length Eagle Creek. Additionally, we assumed a uniform tracer concentration at the inlet section of the channel, which for each test case was prescribed to match to that of the field measurements. At the downstream end of the domain, Newman outlet boundary condition is employed for all three velocity components and tracer concentration.

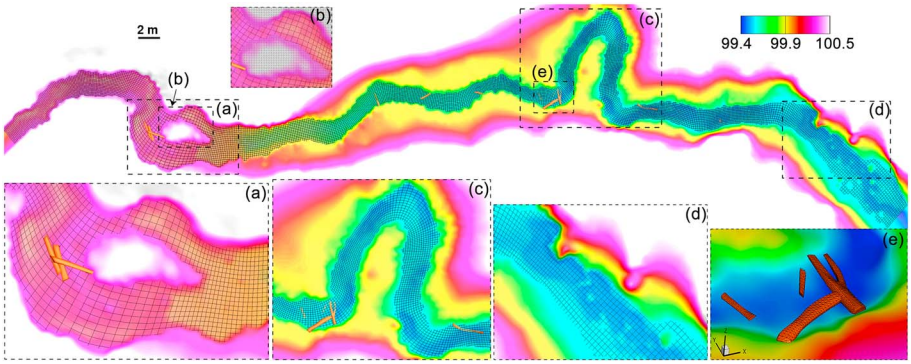

Figure 4. Schematic of the CURVIB approach employed in Eagle Creek. (b–e) Stream bathymetry and large woody debris are embedded in the background domain that is discretized with a structured curvilinear mesh (black lines) (as shown in Figure 3f). (b) The unstructured grid we used to mesh the geometry of the stream bathymetry and the island. For clarity, the structured curvilinear mesh is not shown in Figure 4e. Color scale shows contours of bed elevation in meters (above an arbitrary datum).

The measured water surface is prescribed in the VSL3D model (see Figure 3e) as the water surface sloping rigid-lid boundary condition. This rigid-lid assumption for the free surface boundary condition is justified by the relatively low Froude number of the streamflow. For the solute concentration (volume fraction, ψ) at the free surface and the interface of water and rigid walls (e.g., streambed, side banks, and large woody debris) we employ a Newman, zero-gradient boundary condition [*Wu et al.*, 2000; *Zedler and Street*, 2001, 2006].

The interfaces between water and the surveyed bathymetry of the bed and banks and the geometry of large woody debris are discretized with an unstructured triangular mesh and treated as immersed boundaries using the CURVIB method in VSL3D [*Kang et al.*, 2011]. The background domain (see Figure 3f), within which the resulting digital elevation model of Eagle Creek meandering stream bathymetry and wood pieces are immersed, is discretized with a curvilinear grid system. The curvilinear grid system follows the curves of the stream as required by the CURVIB method [*Kang et al.*, 2011] (see Figures 3 and 4). The wall modeling is used to compute the velocity boundary conditions at the IB nodes since the current simulation does not resolve the viscous sublayer. It is important to emphasize that in the wall model we incorporate the effective roughness height that is locally approximated along the stream (see section 4.2). However, many of the most effective bed roughness elements including larger cobbles and bank irregularities are surveyed, and the computational grid we employ is sufficiently fine so that we can directly resolve most of the key geometric features of Eagle Creek. As such, we treat the bed bathymetry as a rough wall and the presence of larger roughness elements are incorporated by directly resolving the flow structures around them. To investigate the sensitivity of the

Table 3. The Computational Grids and the Time Steps Used for Each Grid System[a]

	Grid I	Grid II
$N_x \times N_y \times N_z$	$2761 \times 101 \times 53$	$3501 \times 133 \times 53$
N_b	556,148	556,148
N_w	1,864	1,864
$\Delta x(m)$	4×10^{-2}	3×10^{-2}
$\Delta y(m)$	2.5×10^{-2}	1.9×10^{-2}
$\Delta z(m)$	5×10^{-3}	5×10^{-3}
Δz^+	45	45
Δt^*	10^{-2}	2.5×10^{-3}

[a] N_i and Δi indicate the number of grid nodes and the grid spacing in the i direction, respectively. N_b is the number of nodes used to discretized the unstructured triangular mesh at the interface of water and rigid bed and banks. N_w is the average number of nodes used to discretized the unstructured triangular mesh at the interface of water and rigid large woody debris (13 pieces total). t^* is the nondimensional time defined as $t^* = tU_m/H_m$. Grid systems are uniform in vertical (z) direction while they are slightly stretched in the streamwise (x) and spanwise (y) directions. $\Delta z^+ = \rho u_* \Delta z/\mu$ is the minimum grid spacing in the vertical direction scaled in inner wall units. Shear velocity, u_*, is calculated from wall model calculations.

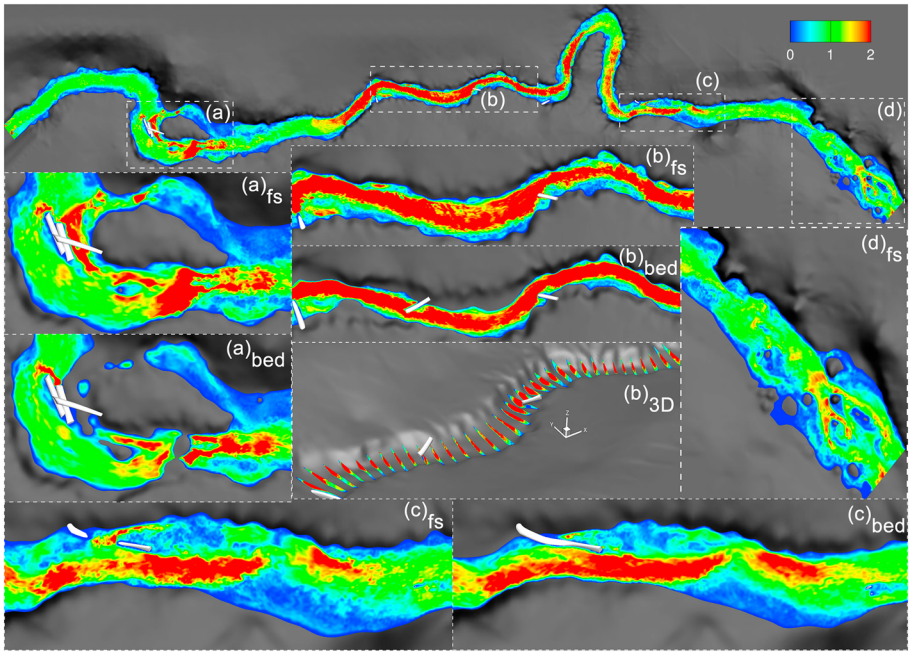

Figure 5. Simulated instantaneous velocity magnitude at $t = 28$ min (roughly two flow-through times). Color scale shows velocity magnitude nondimensionalized by the mean flow velocity (= 0.16 m s^{-1}). "fs" and "bed" subscripts show the free surface and near-bed planes, respectively. "3-D" subscript shows the 3-D view of the selected window in which the z coordinate is exaggerated by a factor of 2.5. The empty gray areas in panels $(a)_{bed}$, (d), $(d)_{bed}$, and $(d)_{fs}$ are locations where the velocity plane passes through solid boundaries (boulders, channel topography) for which velocity is undefined. Flow is from left to right.

computed solutions to grid density, we carried out simulations on two, successively finer, background grid systems, denoted as grids I and II. For both grid systems, the grid nodes are uniformly spaced in the vertical and slightly stretched in the horizontal. An appropriate nondimensional time step $\Delta t^* = \Delta t(U_m/H_m)$ is selected such that the maximum Courant-Friedrichs-Lewy number is less than 1.0. Grid parameters and the time step used for each grid are summarized in Table 3.

The simulations were performed on a Linux cluster composed of 2320 AMD Opteron 2.6 GHz processors. One hundred sixty processors were used for each simulation. The LESs with both grids I and II were first run for only the flow field until the total kinetic energy in the computational domain reached steady state. An instantaneous flow field from these statistically stationary flows for each grid system was used as the initial condition to start the solute transport simulation. The CPU times for the simulations on grids I and II (until the statistical steady state was reached) were about 2.5 and 7.5 days, respectively.

7. Simulation Results

In this section we discuss the computed results and analyze the physics of the turbulent flow and conservative tracer concentration for the test cases A and B. We begin by validating the flow field computations of VSL3D model. The sensitivity of simulated results to grid resolutions is investigated for both flow and concentration field computations, although we note that the field measurements do not provide sufficient information to validate the spatial details of current LES simulations, and thus, we only test the validity of our numerical results using the locally measured data (for additional details regarding flow field validations of VSL3D model, the reader is referred to *Kang et al.* [2011] and *Kang and Sotiropoulos* [2011, 2012a, 2012b]). Next, we present the simulation results of tracer transport along the selected reach of Eagle Creek. More specifically, we compare the measured and computed tracer time series that are probed at two local points along the stream—one near the inlet and one near the outlet of the reach. Finally, we discuss the effect of different objects (e.g., large woody debris, stream bank geometry, and stream bifurcation) on the flow field and residence time of the tracer. All simulations are carried out on two successively refined grids (Table 3); however, the figures only show snapshots of simulated results on the finer grid, grid II.

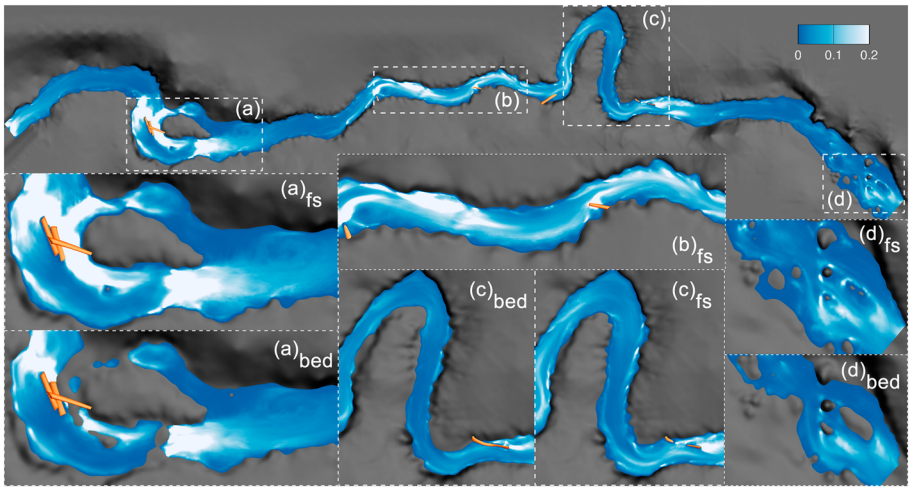

Figure 6. Simulated color maps of tke after time averaging the resolved flow field for approximately 1/14 flow-through time period. Color scale shows tke nondimensionalized by the square of mean flow velocity (U_m^2). fs and bed subscripts show the free surface and near-bed planes, respectively. The empty gray areas in panels $(a)_{bed}$, (d), $(d)_{bed}$, and $(d)_{fs}$ are locations where the velocity plane passes through solid boundaries (boulders, channel topography) for which velocity is undefined. Flow is from left to right.

7.1. Resolved Flow Field

Figure 5 shows snapshots of the computed instantaneous velocity magnitude after $t = 28$ min, i.e., about two flow-through times, at two elevations, including the free surface and a near-bed plane. We note that one flow-through time is the duration of time it takes for a water particle to travel from the inlet to the outlet section of the domain, which is approximated using the mean flow velocity of $U_m = 0.16$ m s^{-1} and the total length of the stream (∼135 m) to be equal to 14 min. As one can see in this figure, the LES resolves complex flow features that are the result of the complex and highly heterogeneous bathymetry, including intense shear layers and many regions of recirculation. The snapshots of the simulated flow near the bed, banks, and the large woody debris clearly demonstrate the ability of the VSL3D to simulate complex flow patterns, e.g., high-velocity streaks and vortex shedding, around discrete roughness elements and immersed objects. More specifically, two main recirculation types can be identified in the simulations. A large-scale recirculation area created immediately downstream of the island near the left bank (see Figure 5). The flow rate on the left branch of the bifurcation is less than 5% of the total flow rate, and therefore, the main recirculation zone is associated with very low velocities and creates a local cavity-like hydrodynamic environment. The simulations also capture numerous small-scale and local recirculation zones near both banks, which are induced by irregular protrusions on the bank geometry.

The cavity-like, small- and large-scale recirculation zones near the banks (e.g., see Figure $6(b)_{bed}$) can be also identified by the shear layers that delineate the local slow-moving flow from the high-speed outer flow through the stream. The resulting high mean shear regions lead to high production of turbulence kinetic energy (tke) as clearly evident in Figure 6, which shows the computed contours of tke at two different planes (near the water surface and near the bed, respectively). Regions with high tke, which represent shear layers with different size, can be observed near three distinct zones within the stream: (i) regions with shallow water depth and large roughness elements (see Figures 6a and 6d), (ii) around large woody debris (Figure 6b), and (iii) regions near the banks where irregularity of the bank geometry introduces protrusions into the flow field (Figure 6c). All these complex local geometric features induce regions of large mean shear and slowly evolving coherent flow structures (which are evident in Movie S1 (Flow Field.avi) in the supporting information) that lead to production of high tke levels. As we will show in a next section, these three features also affect the residence time of the tracer in the stream.

In Figure 7a we show the color map of time-averaged (for approximately 60 s of physical time, which is about 1/14 of a flow-through time) velocity magnitude at the water surface. This figure clearly underscores the highly heterogeneous flow environment created as a result of the complex bathymetry and geomorphic and wood features. Complex flow features arise across a range of scales in this natural environment: from the scale

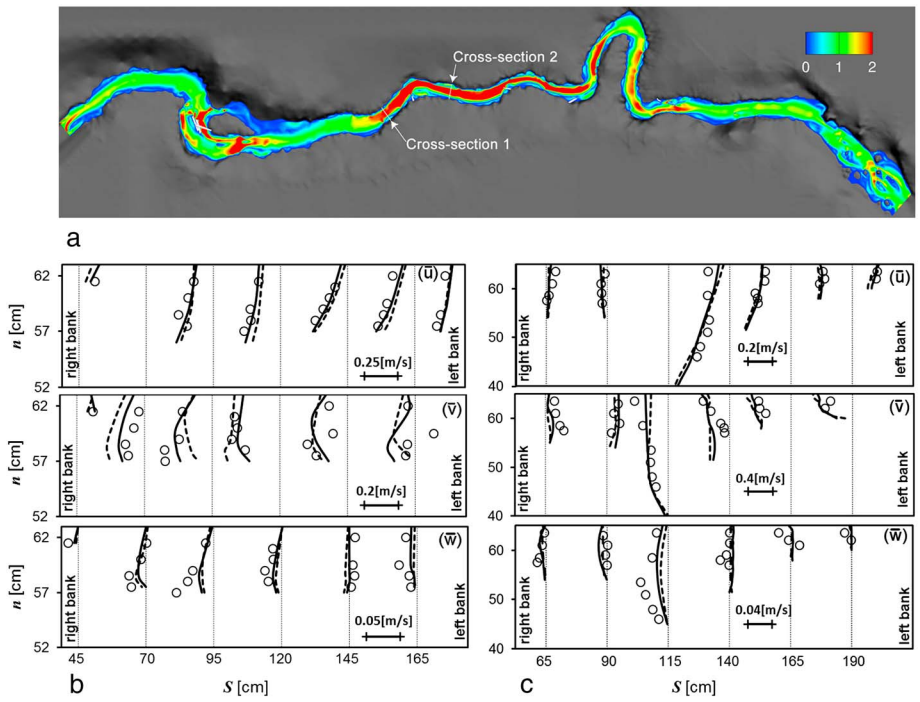

Figure 7. (a) Color map of the computed time-averaged velocity magnitude at the free surface and (b and c) comparison of the measured and computed profiles of the time-averaged streamwise ($\overline{u}$), spanwise ($\overline{v}$), and vertical ($\overline{w}$) velocity components at the two selected cross sections shown in Figure 7a. Circles, dashed lines, and solid lines represent measurements, LES simulations on grids I and II, respectively. Color scale in Figure 7a shows velocity magnitude nondimensionalized by the mean flow velocity (= 0.16 m s^{-1}). ***n*** and ***S*** show the vertical and spanwise coordinates of each cross section. Flow is from left to right.

of the small island near the inlet, to the scale of individual wood pieces, down to the scale of microprotrusions along the banks. At all (of) these scales a similar baseline flow pattern repeats itself: a low-momentum region in the recirculation zone delineated by the high-speed local outer flow. These local cavity-like microflow environments play a major role in trapping passive tracers for a long time and determining the overall residence time of solute within the entire reach (see section 8 and Movie S4 in the supporting information).

In Figure 7a we also show two selected cross sections within the stream reach where measured profiles of three velocity components and turbulence statistics ($\overline{u'v'}$ and $\overline{u'w'}$, where u', v', and w' are the fluctuating velocity components along the streamwise, spanwise, and vertical directions) are compared with the computed/time-averaged results in Figures 7b, 7c, and 8. As one can see in these figures, the simulations capture the velocity component profiles with reasonable accuracy. The agreement between the measured and computed Reynolds stress profiles is not as good as those for the velocity components, but the level of consistency between measured and simulated quantities is especially encouraging when one takes into account the complexity of the stream geometry, inherent uncertainties in defining the local stream geometry and carrying out measurements in a stream like Eagle Creek, and the fact that the simulations were carried out without any calibration with the measured data. Skill score values for LES results of the three velocity components in the streamwise, spanwise, and vertical directions on grid I are 0.95, 0.79, and 0.75, respectively (for definition of skill score see section 7.2). Skill score values for computed $\overline{u'v'}$ and $\overline{u'w'}$ on grid I are 0.68 and 0.71, respectively.

7.2. Test Case A: Pulse Tracer

For this test case, the experiment was performed by releasing the conservative tracer for only 32 s of physical time (i.e., about 1/28 flow-through time). We define the positive and negative wave of solute concentration as a surge of diluted water with tracer concentration of $\psi = 1$ and $\psi = 0$, respectively. Once the injection is halted, a negative wave of tracer concentration (i.e., incoming flow of fresh water, which carries no solute) travels downstream and exits the domain from the outlet section (see Figures 5 and 7a).

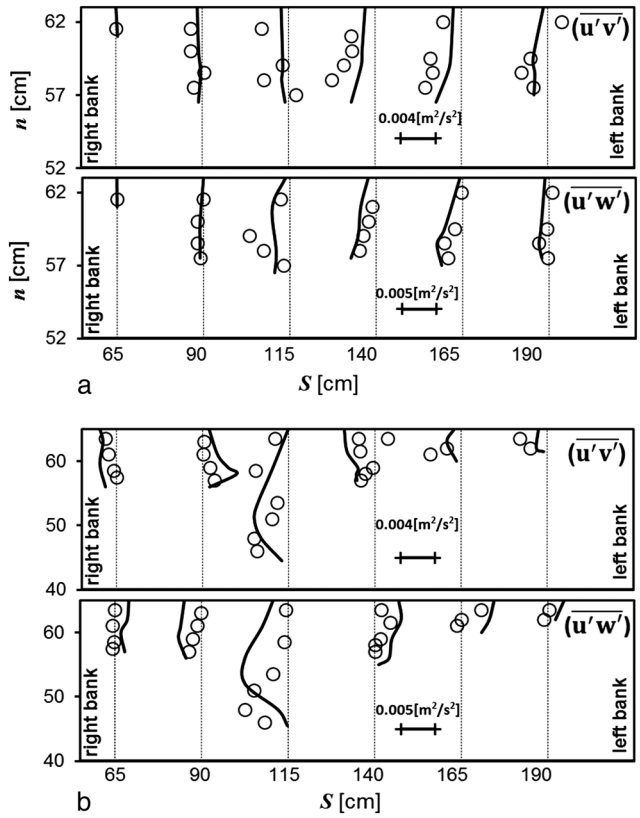

Figure 8. Comparison of the measured and computed profiles of turbulence statistics, $\overline{u'v'}$ and $\overline{u'w'}$, where u', v', and w' are the fluctuating velocity components along streamwise, spanwise, and vertical directions at the two selected cross sections shown in Figure 7a. Circles and lines represent measurements and simulations on grid II, respectively. ***n*** and ***S*** show the vertical and spanwise coordinates of each cross section.

A scenario identical to the experiment of test case A was simulated on the coarse and fine grid systems (see Table 3). The tracer concentration at the inlet cross section is normalized and uniformly fed into the computational domain. Simulations on both grids are continued until the negative wave of tracer concentration exits the outlet section, and after approximately 1700 s the tracer concentration at the outlet, ψ_{outlet}, is less than 10^{-3}. A visual display of the simulated solute transport for this test case can be seen in Movie S2 (Pulse Tracer.avi) in the supporting information.

In Figure 9 we plot the computed snapshots of instantaneous tracer concentration contours along the stream and at the middepth plane. The negative wave of the tracer concentration propagates downstream immediately after the injection is halted. The presence of roughness elements and side bank protrusions create complex transport processes, trapping the tracer for long times (relative to tracer concentration transported by the mean flow in the middle of the stream) and enabling mixing to take place by intense large-scale eddies at the shear layer marking the local cavity-like flow environments (see Movie S2 (Pulse Tracer.avi) in the supporting information). The effect of side bank protrusions in trapping tracer can be clearly seen in Figures 9b–9i. This is especially evident at the most upstream portion of the tracer plume, where there are two distinct branches of tracer adjacent to the side banks. These relatively thin layers of tracer concentration are those that are trapped into the side bank protrusions and gradually released into the main flow (long after the tracer in the middle of the stream is washed out).

Similarly, the regions of recirculation and large-scale local motions in the wake of wood pieces and larger roughness elements increase the residence time and local mixing rate of tracer. The recirculation zone downstream of the island has a pronounced effect on trapping the tracer as can clearly be seen in Figures 9g and 9h. This large recirculation zone traps the material for as long as 24 min, which is about twice the flow-through time (see Movie S2 (Pulse Tracer.avi) in the supporting information).

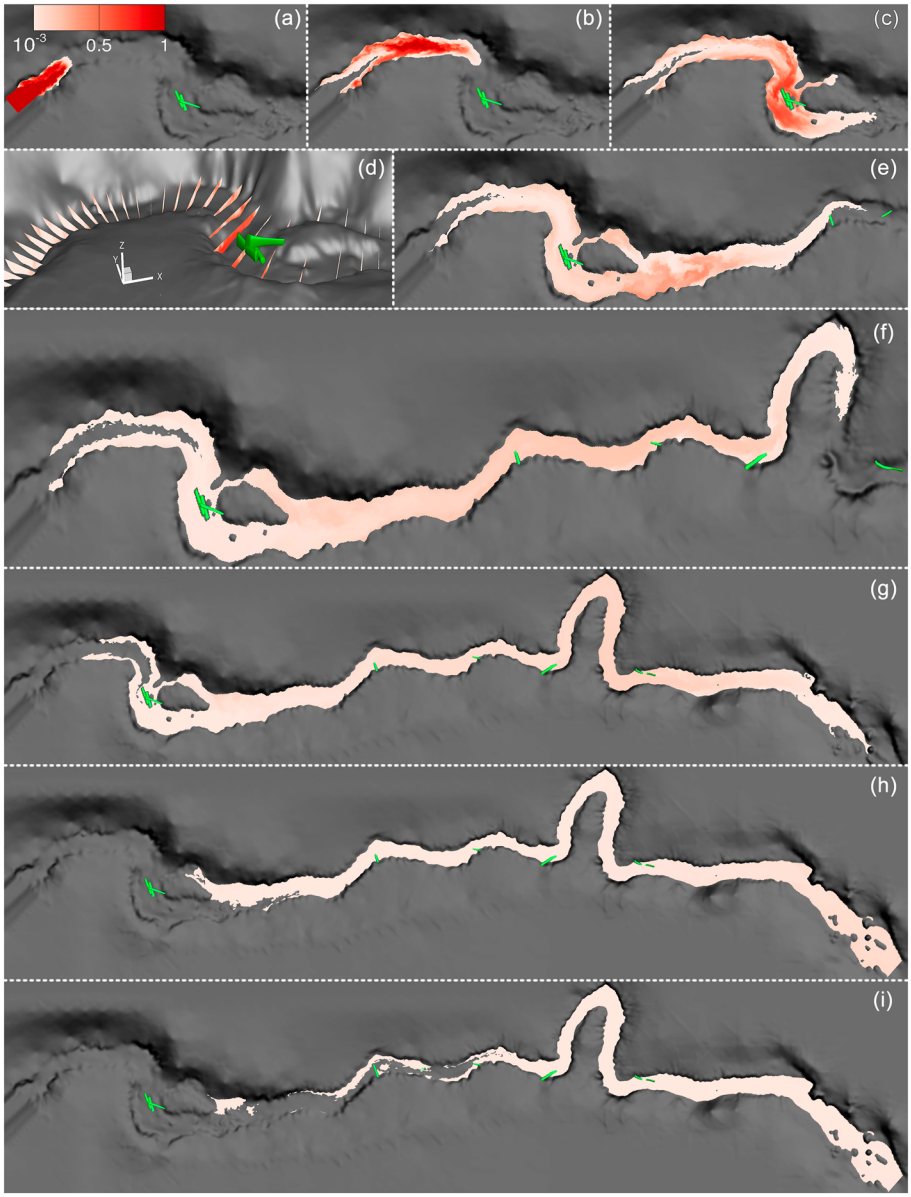

Figure 9. Simulated color maps of instantaneous tracer concentration at middepth plane for test case A after (a) $t = 1/2$ min, (b) $t = 3/2$ min, (c) $t = 3$ min, (d) $t = 3$ min, (e) $t = 6$ min, (f) $t = 9$ min, (g) $t = 13$ min, (h) $t = 19$ min, and (i) $t = 24$ min. z coordinate in Figure 9d is exaggerated by a factor of 2.5. The tracer feeding is stopped after $t = 8/15$ min. Color scale shows tracer concentration in volume fraction. Body of flowing water is not shown, and tracer concentrations below 10^{-3} are cut off. Flow is from left to right.

To demonstrate the accuracy and grid sensitivity of the simulations, we compare the simulated (on both grids) and measured time series of the tracer concentration at the upstream and downstream probe locations (for probe locations see Figure 2). In Figure 10a we compare the tracer concentration measured in the field with the simulated one for the upstream probe (which is about 10 m downstream of the inlet section). A sharp rise in the simulated tracer concentration occurs at $t \sim 50$ s, while the measurements show a somewhat more gradual but of equal magnitude increase in concentration during the same period of time. We argue that the steep increase in the simulated concentration should be attributed to the assumption of fully mixed cross-section profile that we made at the inlet boundary condition. This assumption is obviously not strictly met as it is not necessarily applicable to the case of the measurement where the local turbulent flow might have altered somewhat the cross-sectional distribution of the solute concentration. Nonetheless, on both grid

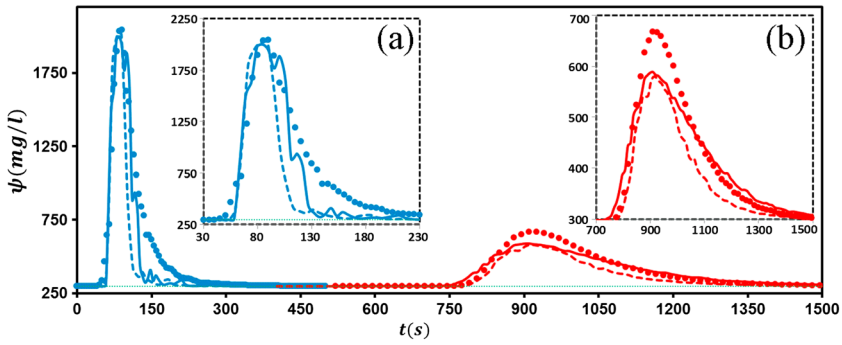

Figure 10. Measured (circles) and simulated time series of tracer concentration for the test case A. The blue and red represent the time series for upstream and downstream probes, respectively. Solid and dashed lines are the simulated time series on grids I and II, respectively. The background graph shows the total time of injection. The selected windows correspond to the (a) upstream and (b) downstream probes, respectively.

systems the simulations are able to reasonably predict all of the characteristics of the wavefront of the tracer concentration within a very complicated and highly 3-D flow environment.

Figure 10b shows the measured and computed concentration time series at the downstream probe location. As one can expect, the downstream probe shows a lower tracer concentration peak over a longer time period. The travel time of the concentration wave, which collectively accounts for the residence time of the tracer along the entire stream, is predicted with reasonable accuracy on both grid systems (maximum calculated discrepancy is less than 7%) with the overall accuracy of the simulated results consistently increasing on the finer grid.

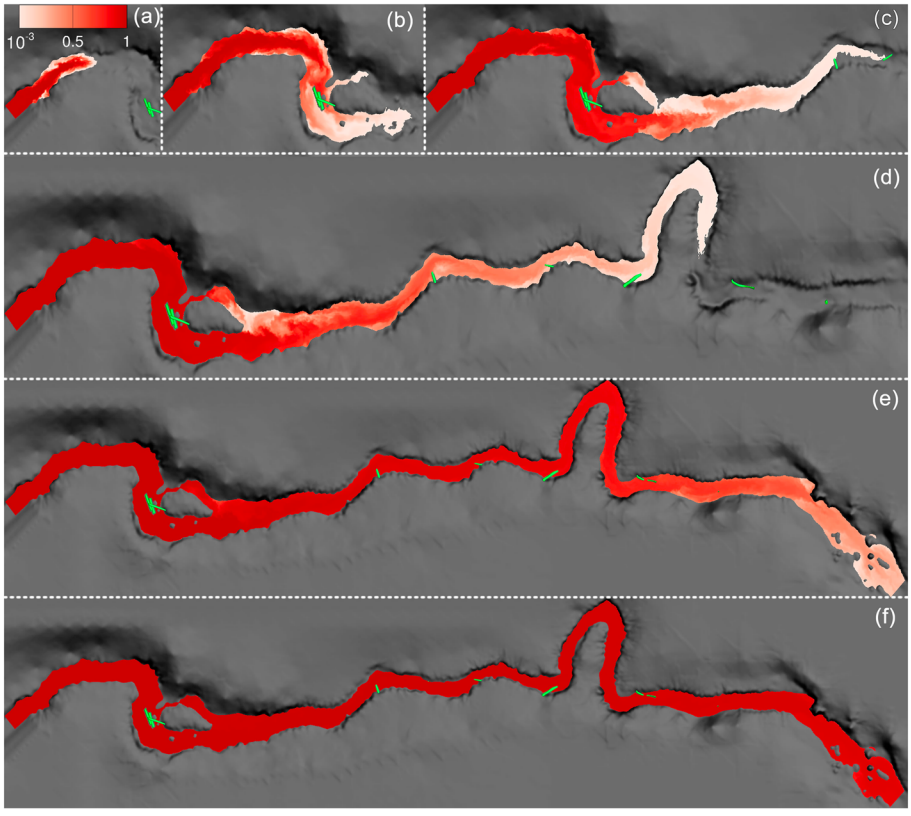

Figure 11. Simulated color maps of instantaneous tracer concentration at middepth plane for test case B after (a) $t = 1$ min, (b) $t = 3$ min, (c) $t = 6$ min, (d) $t = 10$ min, (e) $t = 15$ min, and (f) $t = 20$ min during which the tracer is continuously fed at the inlet. Color scale shows tracer concentration in volume fraction. Body of flowing water is not shown, and tracer concentrations below 10^{-3} are cut off. Flow is from left to right.

The simulations, however, somewhat underpredict the peak of the concentration at the downstream station on both computational grid systems. We argue that this discrepancy can be related to two factors. First, the location of the probe in the field measurements was actually 0.055 m above the bed. Note that even a slight discrepancy in the elevation of the probe can lead to significant variability in the measured time series of the solute concentration. To examine the validity of this hypothesis, we extract the simulation results at a point that is ~0.02 m above the probe location reported in the measurements, and the results for this point indeed show a higher peak concentration closer to the measured value (see below for quantitative comparisons). Second, the use of the WENO scheme (which is excessively diffusive) to discretize the convective terms of the convection-diffusion equation (equation (3)) can also induce extradispersion and consequently underprediction of the tracer concentration peak.

Note that the field measurements have a sampling interval of 5 s to 10 s, which acts to average out sharp jumps in the time series of tracer concentration (see section 5.1 for details of the tracer measurement approach). However, the sampling intervals in the simulations (at both sensor locations) are 0.0094 s and 0.0023 s for grids I and II, respectively (corresponding to the temporal step of each grid system in Table 3). To have a fair comparison between the measured and simulated time series, we compute a low-pass-filtered time series of simulation results to match the sampling frequency of the measured data. Nevertheless, several fluctuations in the simulated time series still exist (see Figure 10a), which suggests that a wide range of energetic turbulent eddies (resolved by the LES) affect the tracer transport. The resolved large eddies travel through the probe location and entrain large amounts of tracer resulting in jumps in the concentration time series. The fluctuations in Figure 10a seem to have an advective time scale of approximately 15 s, which is roughly equal to the time scale of the largest eddy in the stream, approximated as $U_m B = 0.16\ \mathrm{m\ s^{-1}} \times 2.5\ \mathrm{m} = 15\ \mathrm{s}$. Several fluctuations with approximately similar amplitudes can also be seen for the measured tracer concentration (e.g., see the blue circles in Figure 10a at around $t = 150$ s). As tracer feeding is halted and the no-injection phase starts, eddies at the upstream probe location carry more fresh water with $\psi \approx 0$ and affect the fluctuating time series of the tracer concentration (Figure 10a). For the downstream probe, the entire domain is already filled with some level of tracer concentration (see Figures 9e–9h), implying that the traveling large eddies cannot significantly alter the existing concentration field. Therefore, the intensity of the fluctuations observed for the upstream probe location is not expected to be matched at downstream locations (see Figure 10b). The comparison between the simulation results with the two grid systems in Figures 10a and 10b also demonstrates the level of grid sensitivity of the simulation. Overall, while the accuracy on both grids is comparable, the agreement between simulations and measurements increases as the grid is refined.

To quantify the discrepancy between the measured and computed time series of the solute concentration, we statistically analyze the error percentages for each grid system. To do so, we employed the skill score (S_s), which is defined as follows [*Wang et al.*, 2011]:

$$S_s = 1 - \frac{\sum(\psi_{\mathrm{model}} - \psi_{\mathrm{exp}})^2}{\sum(\psi_{\mathrm{exp}} - \overline{\psi_{\mathrm{exp}}})^2} \tag{5}$$

where ψ_{exp} is the measured solute concentration (time-averaged over 5 s and 10 s time interval for the upstream and downstream stations, respectively), ψ_{model} is the computed solute concentration (low pass filtered to match the sampling frequency of ψ_{exp}), and $\overline{\psi_{\mathrm{exp}}}$ is the mean value of ψ_{exp}. The computational error is less for the simulation on grid II than the simulation on grid I, and subsequently, S_s for simulations on grid II (0.94) is higher than that of grid I (0.86). Elevating the position of the probe in the simulations by only 0.02 m in vertical direction leads to skill scores of 0.88 and 0.96 for grids I and II, respectively.

7.3. Test Case B: Plateau Tracer

The experimental procedure for this case was performed by feeding the conservative tracer for ~8 h. A scenario identical to the experiment of test case B was simulated using both grid systems (Table 3). The tracer concentration at the inlet cross section is normalized and uniformly fed into computational domain, as case A. Simulations for this case continued until the solute concentration was uniformly elevated (i.e., 20 min of physical time that is about 7/5 flow-through time) during which ~17 min (~6/5 flow-through time) is required for the peak of the tracer concentration to completely exit the domain. After 20 min the injection is stopped and downstream propagation of the negative wave is simulated for another 15 min until the tracer concentration at the outlet, ψ_{outlet}, is less than 10^{-3}. For a better visual display of the simulated solute transport in this test case, the reader is referred to Movie S3 (Plateau Tracer.avi) in the supporting information.

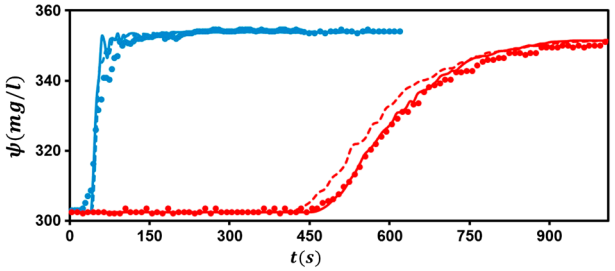

Figure 12. Measured (circles) and simulated time series of tracer concentration for the test case B during continuous feeding (ascending time series). The blue and red represent the time series for upstream and downstream probes, respectively. Solid and dashed lines are the simulated time series on grids I and II, respectively.

In Figure 11 we plot the computed snapshots of instantaneous tracer concentration at the middepth plane during the time period of continuous release. It can be seen from this figure that the positive wave of tracer concentration propagates along the stream until a uniform concentration of $\psi = 1$ covers the entire domain. Like test case A, roughness elements and side banks protrusion along with the large woody debris cause complex transport and mixing processes responsible for the downstream propagation of the wave of tracer concentration. The whole process of propagation until the solute concentration at the inlet equals to its value at the exit takes about 20 min (see Figure 11f). Figure 12 shows the ascending limb of the tracer concentration time series (the sampling frequencies of simulated time series are matched with those of measured data). The computed and measured time series of the tracer concentration at the two upstream and downstream probe locations (see Figure 2) for the first 1000 s is shown in Figure 12. Similar to the test case A, the computed time series at the upstream probe location shows a sharp rise in the tracer concentration at $t \sim 50$ s (Figure 12), while the measured time series shows a more gradual trend. As we discussed for the test case A, the discrepancy may be attributed to the fact that at the inlet boundary condition in the simulation we assume a fully mixed tracer concentration. The comparisons between the simulation results on the two grid systems in Figure 12 also illustrate the grid sensitivity of the simulations with overall trends similar to those discussed for case A.

After the tracer injection is stopped, the negative wave of concentration propagates downstream, and after about 15 min it leaves the domain (Figure 13). During the descending limb of the tracer concentration, trapping of the tracer in various recirculation regions within the stream acts to retain the tracer for a long time within the investigated domain. The corresponding time series for the descending concentrations for both probe locations (see Figure 2) are also shown in Figure 14 where the concentration decreases over a time period of about 15 min to values less than 10^{-3}. We note that the discrepancy between simulation results on grids I and II is pronounced in this figure, especially at the downstream probe location where the coarser grid, grid I, shows a longer mean residence time. It is important to mention that we only simulate 15 min of the negative tracer concentration wave propagation when ψ_{outlet} becomes less than 10^{-3}. Concentration values below 10^{-3} are also graphically cut off in Figure 13. Thus, we argue that the cumulative transient effects in such a stream would persist for a significantly longer time (see Movie S3 (Plateau Tracer.avi) in the supporting information).

To examine the discrepancy between the measured and simulated results for the tracer concentration in this case, we also statistically analyzed the error percentages. Like test case A, the computational error is less for the simulation on grid II than the simulation on grid I. Skill score values for simulations on grids I and II are 0.92 and 0.98, respectively (see equation (5)).

Fluctuations in the tracer concentration, similar to test case A, can be observed in the time series of tracer concentration for this case (see Figures 12 and 14). First, we focus our attention to the descending limb of the time series of tracer concentration (the so-called no-injection phase). During this time period, large fluctuations in the simulation results on both grids can be seen for the upstream probe location (see the solid and dashed blue lines in Figure 14). Such fluctuations with a slightly smaller amplitude can also be recognized in the measured time series from the same probe (see the blue circles in Figure 14). Once again, we argue that the sharp

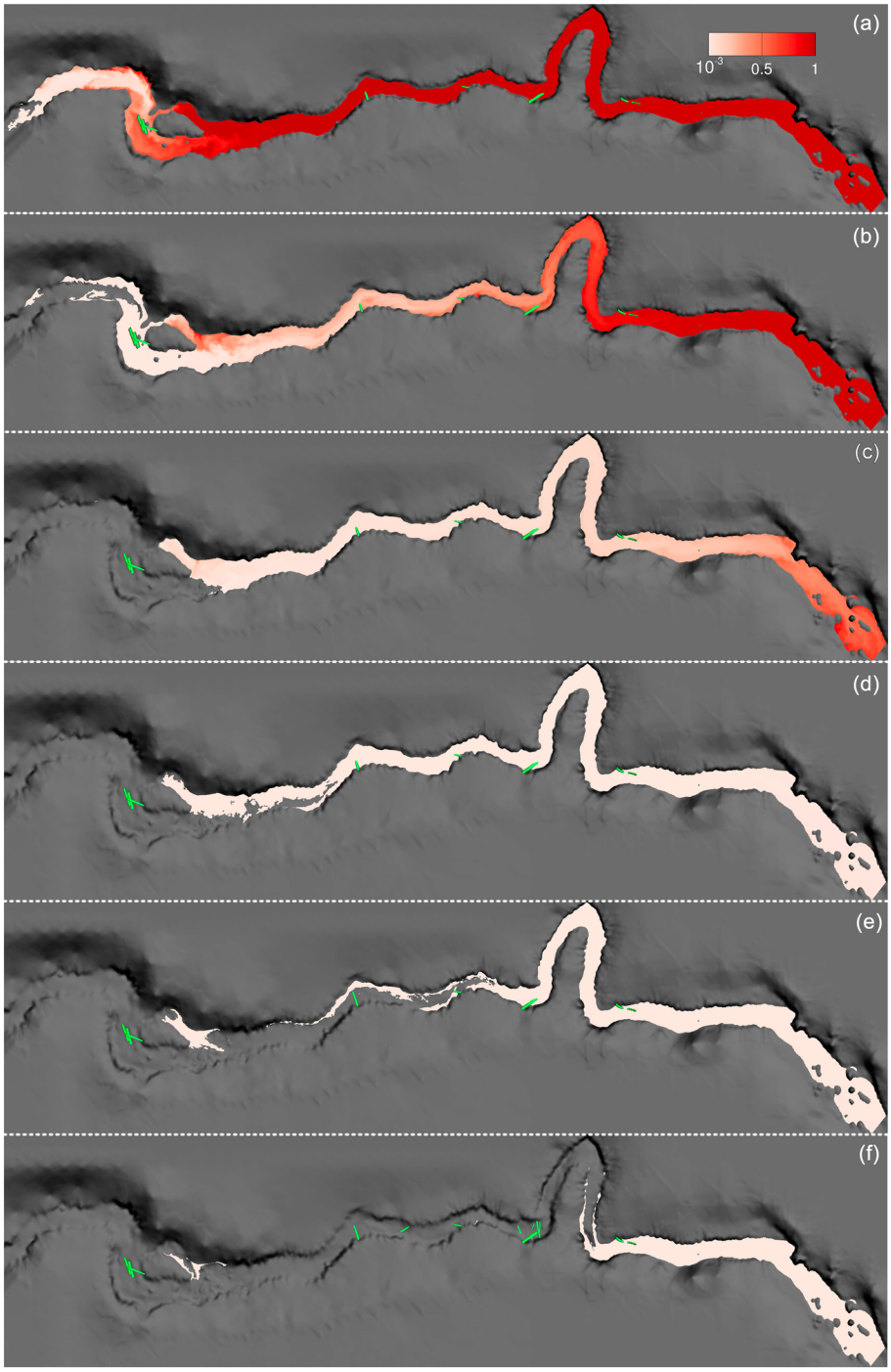

Figure 13. Simulated color maps of instantaneous tracer concentration at middepth plane for test case B after (a) $t = 21$ min, (b) $t = 24$ min, (c) $t = 29$ min, (d) $t = 32$ min, (e) $t = 33$ min, and (f) $t = 34$ min during which the tracer injection at the inlet is stopped. Color scale shows tracer concentration in volume fraction. Body of flowing water is not shown, and tracer concentrations below 10^{-3} are cut off. Flow is from left to right.

gradients in tracer concentration are due to the presence of large-scale eddies passing though the probe location. These eddies at this specific location carry fresh water (as tracer feeding is halted and no-injection phase is started) with a $\psi \approx 0$ and induce significant instantaneous fluctuations in the tracer concentration. Regarding the downstream probe during the no-injection phase, however, we stress that the entire domain is already characterized by a fairly uniform, well-mixed tracer concentration (see Figure 11f), and therefore, stopping

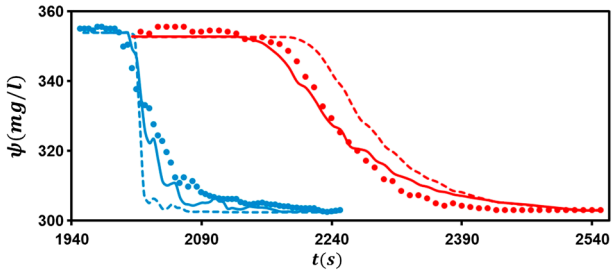

Figure 14. Measured (circles) and simulated time series of tracer concentration for the test case B after feeding is stopped (descending time series). The blue and red represent the time series for upstream and downstream probes, respectively. Solid and dashed lines are the simulated time series on grids I and II, respectively.

the tracer injection would still not allow large eddies to generate appreciable variation in the concentration (see Figure 14).

A similar argument can be also made for the fluctuations in the tracer concentration at the upstream probe location during the injection phase of the tracer (see Figure 12). However, during the ascending limb of the time series the tracer is being injected at the inlet and a positive wave of tracer is approaching the upstream probe. Thus, the large eddies passed the upstream probe and advect high concentration of tracer with a $\psi \approx 1$. The resulting effect in the time series is again intense fluctuations in tracer concentration. On the other hand, for the downstream probe time series during the injection phase, a trend similar to the no-injection phase at downstream probe can be seen (see Figure 12). Overall, tracer concentration fluctuations at the downstream probes have a significantly smaller amplitude than those observed for the upstream probe.

8. Discussion

An effective way to quantify the significance of recirculation regions in controlling the local concentration of the tracer is to calculate and analyze tracer residence time (T_r). T_r is defined as the time required for a fluid particle to exit a specified geometrical domain. It is thus a variable that requires Lagrangian calculations and assumes large values when a particle remains trapped within a zone occupied by persistent slowly rotating eddies such as those observed in the various recirculation regions throughout the stream. If the fluid particle is instead simply advected through the area of interest by a fast-moving flow, as is the case for particles that do not get trapped in recirculating zones, its residence time would be much smaller. For such particles, the dynamics of particle motion are simple and the geometric dimensions of the flow domain along with some average velocity scale would provide reasonable estimates of the residence time. In order to qualitatively illustrate such dynamics, we release 1000 passive particles at a limited plane parallel and 5 mm below the free surface in Eagle Creek. At the beginning particles are uniformly distributed over the plane, which is limited to a region of slow-moving water immediately downstream of the island. As we show in an instantaneous particle release movie (see Movie S4 (Particle Release.avi) in the supporting information), soon after their release particles are advected by small- and large-scale eddies in various directions. Note that this movie is a plan view but some particles plunge down to near-bed regions. As one can see in the movie, depending on their initial location, some particles move faster (following the mean flow in the middle of stream), while some may become trapped or move slower (near stream banks and within circulation regions).

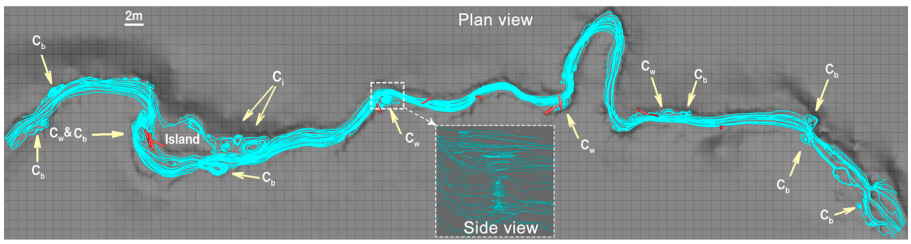

Figure 15. Computed 3-D streamlines of the time-averaged flow field from plan view and a selected secondary flow from side view. The observed recirculation zones are associated with the bed roughness elements and bank irregularity (C_b), large woody debris (C_w), and the island (C_i). Flow is from left to right, and the grid lines are 1 m apart along both directions.

To illustrate the highly heterogeneous distribution of recirculating zones within the stream reach and quantify the spatial extent of these regions and their connection with specific complex features of on the streambed, we plot in Figure 15 the 3-D streamlines of the time-averaged simulation results from plan and side views. Even though in such a complex, unsteady flow, time-averaged streamlines do not correlate with particle trajectories, such a plot helps to illustrate the enormous complexity of the flow within the reach and clearly reveals the presence of multiple regions of recirculating flow, which have the potential to trap tracers for very long times and thus contribute to a dramatic increase in particle residence times. In Figure 15 we have identified each recirculating region as C_j, where the subscript j is related to the specific geomorphologic or wood feature that gives rise to this recirculation region. As is evident from this figure, the recirculation zone C_i, induced by the island, has the largest spatial extent (approximately 5 m in length) and is characterized by multiple eddies. The recirculation zones induced by large woody debris (C_w) are smaller in size (~2 m) but are numerous and should be expected to play a significant role in trapping tracers. We can also clearly observe in this figure the recirculating zones C_b associated with the irregular shape of the stream banks, which further provide multiple regions where tracers can be trapped. The zoomed-in region in Figure 15 shows the tracer trajectory along streamlines in the vertical direction. Spiral-shaped streamlines in this figure are associated with the secondary flows in those zones. The results shown in this figure provide the starting point for the future Lagrangian studies in which the dynamics of each of these recirculating regions will be systematically investigated by introducing ensembles of particles and integrating their trajectories until they finally escape and are released into the main flow, thus enabling the calculation of the residence times associated with each recirculation zone. One such endeavor can be seen in Movie S4 (Particle Release.avi) in the supporting information, while further quantitative analysis of these data is the subject of our next study.

9. Conclusions and Future Work

We illustrated the potential of LES to carry out high-fidelity simulation of turbulent flow and solute transport in a natural stream with complex geometry. To do so, we carried out two different simulations, which correspond to pulse and plateau experiments. Time series of tracer concentration and the turbulent flow field within the study reach were measured and used to validate the simulation results.

The LES results revealed numerous details regarding the mechanisms by which tracers are trapped in local areas, contributing to long residence times in streams. For both tracer feeding scenarios, the simulation results captured most of the experimentally observed tracer concentration time series with reasonably good accuracy, including the overall residence time within the stream, peaks, and propagation time of the tracer concentration.

It is important to mention that even simple 1-D or 2-D models can reproduce time series of solute concentration (albeit at only a limited number of locations and after they undergo extensive calibrations and adjustment using previously measured time series). However, we note that such simple models are not capable of capturing the complex interaction of turbulent flow, solute transport, and intricate stream bathymetry. In contrast, we demonstrated in this study the capabilities of LES to capture complex flow patterns in complex natural streams (without any calibration process) and show the effects of these intricate geometrical characteristics on the transport and trapping of solute concentration. Furthermore, our findings point to the potential of coupling the VSL3D model with detailed field data to develop a powerful, high-performance computing framework for elucidating turbulent flow and transport processes in riverine environments. This approach can thus be extended to address a range of water quality and ecological issues in waterways. These include, among others, understanding how nutrients are processed in streams, how complex geomorphic features alter residence times and promote biogeochemical processes, and how various pollutants will be transported and mixed in any specific environments.

The validated numerical model in this work will be used in a future study to investigate the transport mechanism of a nonconservative solute (e.g., nitrate) in the same stream reach on the East Branch of Eagle Creek. Experimental observations for a nonconservative tracer will also be carried out to develop an appropriate bed boundary condition for nitrate uptake in the numerical model. In addition, to understand the specific contribution of various recirculating regions to stream reach residence time, future work will focus on systematic Lagrangian analysis to calculate residence times of nondiffusive particles.

Acknowledgments
This work was supported by National Center for Earth-surface Dynamics (NCED), the NSF Science and Technology Center that operated from 2002 to 2012, and NSF PIF-BIC grant 1318201. Computational resources were provided by the University of Minnesota Supercomputing Institute. We thank Jovanny Velez and Guelord Mpagazihe for their extensive efforts to survey Eagle Creek and for their assistance with the tracer experiments. We thank Chip Small, Nolan Kleinjan, and Adam Eldeeb for helping to collect data during the tracer experiments. We also greatly appreciate Rob Runkel and Oliver Fringer and the anonymous reviewer for their contributions to improve the quality of this paper. For additional information regarding the data generated from these simulations, the reader can contact Fotis Sotiropoulos via e-mail: fotis.sotiropoulos@stonybrook.edu. The VSL3D model is part of the Virtual Flow Simulator (VFS) suite of computational fluid dynamics solvers developed by the group of Fotis Sotiropoulos. The code is available as open source and can be downloaded, along with supporting documentation, from https://github.com/SAFL-CFD-Lab/VFS-Rivers.

References

Ambrose, R., T. Wool, and T. Barnwell (2009), Development of water quality modeling in the United States, *Environ. Eng. Res.*, *14*(4), 200–210.
Baker, D., B. Bledsoe, and J. Price (2011), Stream nitrate uptake and transient storage over a gradient of geomorphic complexity, north-central Colorado, USA, *Hydrol. Processes*, *26*, 3241–3252, doi:10.1002/hyp.8385.
Bangen, S., J. Wheaton, N. Bouwes, B. Bouwes, and C. Jordan (2014), A methodological intercomparison of topographic survey techniques for characterizing wadeable streams and rivers, *Geomorphology*, *206*, 343–361.
Bernhardt, E., G. Likens, D. Buso, and C. Driscoll (2003), In-stream uptake dampens effects of major forest disturbance on watershed nitrogen export, *Proc. Natl. Acad. Sci. USA*, *100*, 10,304–10,308.
Borazjani, I., L. Ge, and F. Sotiropoulos (2008), Curvilinear immersed boundary method for simulating fluid structure interaction with complex 3D rigid bodies, *J. Comput. Phys.*, *227*, 7587–7620.
Branfireun, B., and N. Roulet (2002), Controls on the fate and transport of methylmercury in a boreal headwater catchment, northwestern Ontario, Canada, *Hydrol. Earth Syst. Sci.*, *6*(4), 783–794.
Brian, P. L. T. (1961), A finite-difference method of high-order accuracy for the solution of three-dimensional transient heat conduction problems, *AIChE J.*, *7*(3), 367–370.
Burnett, R. D., and E. O. Frind (1987), Simulation of contaminant transport in three dimensions: 1. The alternating direction Galerkin technique, *Water Resour. Res.*, *23*(4), 683–694.
Ceola, S., E. Bertuzzo, G. Singer, T. J. Battin, A. Montanari, and A. Rinaldo (2014), Hydrologic controls on basin-scale distribution of benthic invertebrates, *Water Resour. Res.*, *50*(4), 2903–2920, doi:10.1002/2013WR015112.
Cerco, C., and T. Cole (1993), Three-dimensional eutrophication model of Chesapeake bay, *J. Environ. Eng.*, *119*(6), 1006–1025.
Cerco, C., M. Noel, and S. Kim (2006), Three-dimensional management model for Lake Washington: Part II. Eutrophication modeling and skill assessment, *Lake Reservoir Manage.*, *22*(2), 115–131.
Cerco, C., T. Threadgill, M. Noel, and S. Hinz (2013), Modeling the pH in the tidal fresh Potomac River under conditions of varying hydrology and loads, *Ecol. Modell.*, *257*, 101–112.
Chang, K. S., G. Constantinescu, and S. Park (2007), The purging of a neutrally buoyant or a dense miscible contaminant from a rectangular cavity. Part II: The case of an incoming fully turbulent overflow, *J. Hydraul. Eng.*, *133*, 373–385.
Chou, Y. J., and O. B. Fringer (2008), Modeling dilute sediment suspension using large-eddy simulation with a dynamic mixed model, *Phys. Fluids*, *20*, 115103.
Chou, Y. J., and O. B. Fringer (2010), A model for the simulation of coupled flow-bed form evolution in turbulent flows, *J. Geophys. Res.*, *115*, C10041, doi:10.1029/2010JC006103.
De Smedt, F., W. Brevis, and P. Debels (2005), Analytical solution for solute transport resulting from instantaneous injection in streams with transient storage, *J. Hydrol.*, *315*(1–4), 25–39.
Demuren, A. O., and W. Rodi (1986), Calculation of flow and pollutant dispersion in meandering channels, *J. Fluid Mech.*, *172*, 63–92.
Ensign, S., and M. Doyle (2005), In-channel transient storage and associated nutrient retention: Evidence from experimental manipulation, *Limnol. Oceanogr.*, *50*, 1740–51.
Fausch, K. D., and R. J. White (1981), Competition between brook trout Salvelinus fontinalis and brown trout Salmo trutta for positions in a Michigan stream, *Can. J. Fish. Aquat. Sci.*, *38*(10), 1220–1227.
Ge, L., and F. Sotiropoulos (2007), A numerical method for solving the 3D unsteady incompressible Navier-Stokes equations in curvilinear domains with complex immersed boundaries, *J. Comput. Phys.*, *225*, 1782–1809.
Gilmanov, A., and F. Sotiropoulos (2005), A hybrid Cartesian/immersed boundary method for simulating flows with 3D, geometrically complex, moving bodies, *J. Comput. Phys.*, *207*, 457–492.
Gooseff, M., R. Hall Jr., and J. Tank (2007), Relating transient storage to channel complexity in streams of varying land use in Jackson Hole, Wyoming, *Water Resour. Res.*, *43*, W01417, doi:10.1029/2005WR004626.
Gooseff, M., D. Benson, M. Briggs, M. Weaver, W. Wollheim, B. Peterson, and C. Hopkinson (2011), Residence time distributions in surface transient storage zones in streams: Estimation via signal deconvolution, *Water Resour. Res.*, *47*, W05509, doi:10.1029/2010WR009959.
Gooseff, M., M. Briggs, K. Bencala, B. McGlynnd, D. T. Scott, and J. Hydrol. (2013), Do transient storage parameters directly scale in longer, combined stream reaches? Reach length dependence of transient storage interpretations, *483*, 16–25, doi:10.1016/j.jhydrol.2012.12.046.
Groffman, P. M., K. Butterbach-Bahl, R. W. Fulweiler, A. J. Gold, J. L. Morse, E. K. Stander, C. Tague, C. Tonitto, and P. Vidon (2009), Challenges to incorporating spatially and temporally explicit phenomena (hotspots and hot moments) in denitrification models, *Biogeochemistry*, *93*(1), 49–77.
Hart, D., and C. Finelli (1999), Physical-biological coupling in streams: The pervasive effects of flow on benthic organisms, *Annu. Rev. Ecol. Syst.*, *30*, 363–395.
Hoch, T., and P. Garreau (1998), Phytoplankton dynamics in the English Channel: A simplified three-dimensional approach, *J. Mar. Syst.*, *16*(1–2), 133–150.
Jiang, G., and C. Shu (1996), Efficient implementation of weighted ENO schemes, *J. Comput. Phys.*, *126*(1), 202–228.
Kang, S., and F. Sotiropoulos (2011), Flow phenomena and mechanisms in a field-scale experimental meandering channel with a pool-riffle sequence: Insights gained via numerical simulation, *J. Geophys. Res.*, *116*, F0301, doi:10.1029/2010JF001814.
Kang, S., and F. Sotiropoulos (2012a), Numerical modeling of 3D turbulent free surface flow in natural waterways, *Adv. Water Resour.*, *40*, 23–36, doi:10.1016/j.advwatres.2012.01.012.
Kang, S., and F. Sotiropoulos (2012b), Assessing the predictive capabilities of isotropic, eddy viscosity Reynolds-averaged turbulence models in a natural-like meandering channel, *Water Resour. Res.*, *48*, W06505, doi:10.1029/2011WR011375.
Kang, S., A. Lightbody, C. Hill, and F. Sotiropoulos (2011), High-resolution numerical simulation of turbulence in natural waterways, *Adv. Water Resour.*, *34*(1), 98–113.
Kaufmann, P., and J. Faustini (2012), Simple measures of channel habitat complexity predict transient hydraulic storage in streams, *Hydrobiologia*, *658*(1), 69–95.
Khosronejad, A. (2009), Optimization of the Sefid-Roud Dam desiltation process using a sophisticated one-dimensional numerical model, *Int. J. Sediment Res.*, *2*, 189–200.
Khosronejad, A., and F. Sotiropoulos (2014), Numerical simulation of sand waves in a turbulent open channel flow, *J. Fluid Mech.*, *753*, 150–216.
Khosronejad, A., A. Salehi, C. Rennie, and I. Gholami (2008), Three dimensional numerical modeling of sediment release in a water reservoir, *J. Hydraul. Res.*, *46*(2), 209–223.
Khosronejad, A., J. L. Kozarek, and F. Sotiropoulos (2014), Simulation-based approach for stream restoration structure design: Model development and validation, *J. Hydraul. Eng.*, *140*(7), 1–16.

Khosronejad, A., J. L. Kozarek, M. L. Palmsten, and F. Sotiropoulos (2015), Numerical simulation of large dunes in meandering streams and rivers with in-stream structure, *Adv. Water Resour.*, *81*, 45–61, doi:10.1016/j.advwatres.2014.09.007.
Kirkpatrick, M. P., and S. W. Armfield (2005), Experimental and les simulation results for the purging of salt water from a cavity by an overflow of fresh water, *Int. J. Heat Mass Transfer*, *48*, 341–351.
Kozarek, J. L., W. C. Hession, C. Dolloff, and P. Diplas (2010), Hydraulic complexity metrics for evaluating in-stream brook trout habitat, *J. Hydraul. Eng.*, *136*, 1067–1076.
Kraft, S., Y. Wang, and M. Oberlack (2011), Large eddy simulation of sediment deformation in a turbulent flow by means of level-set method, *J. Hydraul. Eng.*, *137*(11), 1394–1405.
Lancaster, J., and A. Hildrew (1993), Flow refugia and the microdistribution of lotic macroinvertebrates, *J. N. Am. Benthol. Soc.*, *12*(4), 385–393.
McClain, M., et al. (2003), Biogeochemical hot spots and hot moments at the interface of terrestrial and aquatic ecosystems, *Ecosystems*, *6*(4), 301–312.
McCoy, A., G. Constantinescu, and L. Weber (2007), A numerical investigation of coherent structures and mass exchange processes in channel flow with two lateral submerged groynes, *Water Resour. Res.*, *43*, W05445, doi:10.1029/2006WR005267.
McDonald, C., V. Bennington, N. Urban, and G. McKinley (2012), 1-D test-bed calibration of a 3-D Lake Superior biogeochemical model, *Ecol. Modell.*, *225*, 115–126.
Morales, Y., L. J. Weber, A. E. Mynett, and T. J. Newton (2006), Effects of substrate and hydrodynamic conditions on the formation of mussel beds in a large river, *J. N. Am. Benthol. Soc.*, *25*(3), 664–676.
Opdyke, M. R., M. B. David, and B. L. Rhoads (2006), Influence of geomorphological variability in channel characteristics on sediment denitrification in agricultural streams, *J. Environ. Qual.*, *35*, 2103–2112.
Park, K., H. Jung, H. Kim, and S. Ahn (2005), Three-dimensional hydrodynamic-eutrophication model (HEM-3D): Application to Kwang-Yang Bay, Korea, *Mar. Environ. Res.*, *60*(2), 171–193.
Parsheh, M., F. Sotiropoulos, and F. Porte-Angel (2010), Estimation of power spectra of acoustic Doppler velocimetry data contaminated with intermittent spikes, *J. Hydraul. Eng.*, *136*, 368–378.
Reckhow, K., and S. Chapra (1999), Modeling excessive nutrient loading in the environment, *Environ. Pollut.*, *100*(1–3), 197–207.
Resop, J., J. Kozarek, and W. Hession (2012), Terrestrial laser scanning for delineating in-stream boulders and quantifying habitat complexity, *Photogramm. Eng. Remote Sens.*, *78*, 363–371.
Runkel, R., D. McKnight, and H. Rajaram (2003), Modeling hyporheic zone processes, *Adv. Water Resour.*, *26*(9), 901–905.
Runkel, R. L. (2015), On the use of rhodamine WT for the characterization of stream hydrodynamics and transient storage, *Water Resour. Res.*, *51*, 6125–6142, doi:10.1002/2015WR017201.
Schmalle, G. F., and C. R. Rehmann (2014), Analytical solution of a model of contaminant transport in the advective zone of a river, *J. Hydraul. Eng.*, *140*, 04014029.
Stoesser, T. (2014), Large-eddy simulation in hydraulics: Quo vadis?, *J. Hydraul. Res.*, *52*(4), 441–452, doi:10.1080/00221686.2014.944227.
Stofleth, J. M., D. Shields, and G. A. Fox (2008), Hyporheic and total transient storage in small sand-bed streams, *Hydrol. Processes*, *22*, 1885–1894, doi:10.1002/hyp.6773.
Tank, J., J. L. Meyer, D. M. Sanzone, P. J. Mulholland, J. R. Webster, B. J. Peterson, W. M. Wollheim, and N. E. Leonard (2000), Analysis of nitrogen cycling in a forest stream during autumn using a 15N-tracer addition, *Limnol. Oceanogr.*, *45*, 1013–1029.
Tiedje, J., A. Sexstone, D. Myrold, and J. Robinson (1982), Denitrification: Ecological niches, competition and survival, *A. Van Leeuw. J. Microb.*, *48*(6), 569–583.
Van Rijn, L. C. (1984), Sediment transport. Part III: Bed forms and alluvial roughness, *J. Hydraul. Eng.*, *110*(12), 1733–1754.
Wang, B., S. N. Giddings, O. B. Fringer, E. S. Gross, D. A. Fong, and S. G. Monismith (2011), Modeling and understanding turbulent mixing in a macrotidal salt wedge estuary, *J. Geophys. Res.*, *116*, C02036, doi:10.1029/2010JC006135.
Wu, W., W. Rodi, and T. Wenka (2000), 3D numerical modeling of flow and sediment transport in open channels, *J. Hydraul. Eng.*, *126*(1), 4–15.
Zedler, E. A., and R. L. Street (2001), Large-eddy simulation of sediment transport: Currents over ripples, *J. Hydraul. Eng.*, *127*(6), 444–452.
Zedler, E. A., and R. L. Street (2006), Sediment transport over ripples in oscillatory flow, *J. Hydraul. Eng.*, *132*(2), 1–14.